ADVANCED MATERIALS

Supporting Information

for *Adv. Mater.*, DOI: 10.1002/adma.201405244

Mn_2FeWO_6: a New Ni_3TeO_6-Type Polar and Magnetic Oxide

*Man-Rong Li, Mark Croft, Peter W. Stephens, Meng Ye, David Vanderbilt, Maria Retuerto, Zheng Deng, Christoph P. Grams, Joachim Hemberger, Joke Hadermann, Wen-Min Li, Chang-Qing Jin, Felix O. Saouma, Joon I. Jang, Hirofumi Akamatsu, Venkatraman Gopalan, David Walker, and Martha Greenblatt**

Supporting Information

Mn_2FeWO_6 – a New Ni_3TeO_6-Type Polar and Magnetic Oxide

*Man-Rong Li, Mark Croft, Peter W. Stephens, Meng Ye, David Vanderbilt, Maria Retuerto, Zheng Deng, Christoph P. Grams, Joachim Hemberger, Joke Hadermann, Wen-Min Li, Chang-Qing Jin, Felix O. Saouma, Joon I. Jang, Hirofumi Akamatsu, Venkatraman Gopalan, David Walker, Martha Greenblatt**

Dr. Man-Rong Li, Dr. Maria Retuerto, Dr. Zheng Deng, Prof. Martha Greenblatt
Department of Chemistry and Chemical Biology, Rutgers, the State University of New Jersey, 610 Taylor Road, Piscataway, New Jersey 08854, USA
E-mail: martha@chem.rutgers.edu
Prof. Mark Croft, Ms. Meng Ye, Prof. David Vanderbilt
Department of Physics and Astronomy, Rutgers, the State University of New Jersey, 136 Frelinghusen Road, Piscataway, New Jersey 08854, USA
Dr. Christoph P. Grams, Prof. Joachim Hemberger
II. Physikalisches Institut, Universität zu Köln, D 50937 Köln, Germany
Prof. Joke Hadermann
EMAT, University of Antwerp, Groenenborgerlaan 171, B-2020 Antwerp, Belgium
Prof. Peter W. Stephens
Department of Physics & Astronomy, State University of New York, Stony Brook, New York 11794, USA
Mr. Wen-Min Li, Prof. Chang-Qing Jin
Institute of Physics, Chinese Academy of Sciences, P. O. Box 603, Beijing 100080, China
Mr. Felix O. Saouma, Prof. Joon I. Jang
Department of Physics, Applied Physics and Astronomy, Binghamton University, P.O. Box 6000, Binghamton, New York 13902, USA
Dr. Hirofumi Akamatsu, Prof. Venkatraman Gopalan
Department of Materials Science and Engineering, Pennsylania State University, University Park, Pennsylvania 16802, USA
Prof. David Walker
Lamont Doherty Earth Observatory, Columbia University, 61 Route 9W, PO Box 1000, Palisades, New York 10964, USA

Keywords: multiferroics, Mn_2FeWO_6, polar magnet, magnetic phase diagram, first-principles calculations

Supplementary Text

1. Synthesis and Phase Analysis

Polycrystalline Mn_2FeWO_6 was prepared from stoichiometric mixture of MnO (99.99%, Alfa Aesar), Fe (99.998%, Alfa Aesar), Fe_2O_3 (99.998%, Alfa Aesar), and WO_3 (99.8%, Alfa Aesar) at 1673 K under 8 GPa for 1 h in a Multi-Anvil Press as used in our previous work.[1-4] The pure wolframite $(Mn_{0.8}Fe_{0.2})WO_4$ phase was prepared from stoichiometric mixture of MnO, Fe, Fe_2O_3, and WO_3 at the same conditions to evaluate its contribution to the physical properties. Phase analysis of the prepared samples were performed using the laboratory powder X-ray diffraction (PXD) patterns collected on a Bruker D8 ADVANCE diffractometer (Cu K_α, λ = 1.5406 Å). PXD patterns (**Figure S2a**) of the as-made Mn_2FeWO_6 can be well indexed in a rhombohedral cell with small wolframite impurity as compared with the PXD patterns (**Figure S2b**) of $(Mn_{0.8}Fe_{0.2})WO_4$ woframite phase prepared at the same pressure and temperature.

2. Optical and Microprobe Analysis

Fragments of the obtained Mn_2FeWO_6 phase were embedded in epoxy resin, ground, and then polished for optical and electron microprobe examination. Doubly-polarized incident illumination image (**Figure S3**a) of grain mount reveals that the ~ 1/2 mm grain is almost entirely comprised of a poly-synthetically twinned opaque single crystal. The lamellae are revealed by subtle but well-delimited alternating bands of higher and lower reflectivity. The single crystal nature of the lamellar aggregate is revealed by the consistent orientation throughout the sample of a swarm of cleavage-pluck pits and of the twin lamellae themselves (all horizontal and parallel to the horizontal cleavage set). There is a few percent of an impurity phase of lower reflectivity that shows a deep red-orange internal reflection in favorable orientations. This impurity phase tends to be distributed on the grain margins of the major phase.

The electron microprobe analyses were carried out with a 5 wavelength-dispersive spectrometer Cameca SX-100 that has an additional Princeton Gamma Tech IMIX energy dispersive spectrometer, installed at the American Museum of Natural History in New York City. W metal, Mn-metasilicate, and IL ($FeTiO_3$) were used as standards for W Mα, Mn Kα, Fe Kα, and O Kα radiation. The $FeTiO_3$ ilmenite was not a particularly appropriate standard for direct analysis of O so the oxygen numbers reported are not considered reliable enough to establish O stoichiometry. Our compositions are reported as O_x rather than O_4 or O_6. The relative W, Mn, and Fe amounts are considered reliable at the ±½ % level. No other elements, other than Pt in the wrapper, were determined to be detectably present by energy dispersive analysis.

Microprobe analysis on the main phase (spots 1-3 in **Figure S3**a, **Table S1**) gives a composition of $Mn_2Fe_{0.91(1)}W_{0.96(1)}O_x$, close to Mn_2FeWO_6 but slightly deficient in Fe. The impurity phase (spots 4-6 and 7 in **Figure S3**a) have small content variation but the (Mn + Fe)/W ratio is close to unity and gives $(Mn_{0.79(1)}Fe_{0.21(1)})WO_x$, which is confirmed to be the (Mn,Fe)WO_4 wolframite-type phase (*P*2/*c*, *a* ~ 4.81 Å, *b* ~ 5.75 Å, *c* ~ 4.99 Å, β = 90.89º) [5] from PXD data (**Figure S2**). Fe was present in the Pt-wrap as shown in **Figure S3**b, suggesting reaction between the Pt container and some Fe, since the formation of Pt-Fe alloy is a well-known problem in systems with Pt and Fe/Fe_2O_3.[6] At experimental conditions, the Pt-wrap absorbs Fe to form the Pt-Fe alloy, causing Fe depletion (and oxidation) in the neighboring sample. This Fe loss is only partially accommodated by a shift in composition of the target phase; the depletion beyond the solubility limit of the target phase results in the formation of Fe- poor wolframite phase (Mn/Fe ratio ~ 4 in (Mn, Fe)WO_x). The impurity particles are mainly spread around the edge of sample as a consequence of this Fe loss to the container mechanism. The Fe-poor layer could be thin and only formed on the sample surface area, as no obvious Fe depletion is detected from the following Rietveld refinements on synchrotron powder x-ray diffraction (SPXD) data. However, it is also unlikely that the

refinements would pick up the very small depletions of Fe in the target phase (that we see by microprobe) because the principal manifestation of the depletion is the formation of wolframite. This indicates that the range of stoichiometric variations of (Fe+Mn)/W possible in these oxides through variations of solubility of one in the other is quite limited, in accord with the probe analyses.

3. Electron Diffraction

Electron microscopy studies were carried out to examine the Fe/W ordering/disordering degree. Samples for electron microscopy were prepared by dispersing the powder in ethanol and depositing on a holey carbon grid. Selected area electron diffraction (SAED) patterns were obtained on a Philips CM20 transmission electron microscope. High angle annular dark field scanning transmission electron microscopy (HAADF-STEM) images were recorded on an FEI Titan 80-300 "cubed" microscope operated at 300 kV. The SAED tilt patterns (**Figure S4**a) around the reciprocal directions $[10\bar{1}\bar{2}]$ and $[01\bar{1}\bar{1}]$ show a match with the cell parameters obtained by PXD. The ordering between W (74) and Mn/Fe (25/26) is very clear on the HAADF-STEM images taken along the [100] zone (**Figure S4**b and close-up in **Figure 1**b), because of the large difference in *Z* between them. On the images the columns of W atoms correspond to the very bright dots, while the less bright dots in between are the Mn and Fe columns. For clarity, 2 × 2 unit cells in [100] projection have been placed over the close-up, indicating the positions of the different atom columns. The images correspond to the proposed model with ordering between W and Fe.

4. Synchrotron Powder X-ray Diffraction

Room temperature (RT) SPXD data were recorded on beam line X-16C (λ = 0.70005 Å) at the Brookhaven National Synchrotron Light Source (NSLS). Diffraction data analysis and Rietveld refinement were performed with the TOPAS software package (**Figure S5**).[7]

It is noteworthy that in Mn_2FeMO_6 (M = Sb^{5+}, Nb^{5+}, Ta^{5+}, Mo^{5+} + and W^{6+}) analogs, although all the M ions have similar ionic radii (*r*, **Table S4**), different degrees of cation ordering and structure types are presented. The relatively small size difference between Fe^{3+} ($r(Fe^{3+})$ = 0.645 Å, high spin (HS)) and Sb^{5+} ($r(Sb^{5+})$ = 0.60 Å) leads to disordered Fe/Sb configuration and IL-type structure of Mn_2FeSbO_6.[8] Similarly, disorderd Fe^{3+}/M^{5+} is also observed in Mn_2FeMO_6 (M = Nb, Ta), but the second-order Jahn-Teller (SOJT) effect of the d^0 ions (Nb^{5+} and Ta^{5+}) favors a higher degree of order between the A- and B-site cations, leading to the polar LN-type structure.[4] In contrast, Fe^{3+} (d^5, HS) and Mo^{5+} (d^1, $r(Mo^{5+})$ = 0.61 Å) with comparable sizes, are highly ordered (~ 97%) in the polar NTO-type structure.[3] It is well established that W^{6+} is highly favored at octahedral sites of perovskites and related compounds,[9-11] even in reducing conditions.[12] Thus, in Mn_2FeWO_6 the high oxidation state of W^{6+} ($r(W^{6+})$ = 0.60 Å) forces the oxidation state of Fe^{2+} ($r(Fe^{2+})$ = 0.78 Å), which yields larger cell parameters and volume than those of Mn_2FeMoO_6 (**Table S4**), and a smaller tolerance factor (*t* = 0.855) than other $Mn_2^{2+}Fe^{3+}M^{5+}O_6$ (M = Nb, Ta, Mo, and Sb) corundum-types, and therefore, also requires higher pressure for its preparation.[4, 13]

5.Second Harmonic Generation

The RT broadband second harmonic generation (SHG) measurements were conducted using the method in our previous work.[3] Temperature dependence of the SHG was also measured on a pellet between 10 and 300 K in normal reflection geometry with an 800 nm fundamental input generated by a Ti:saphire laser (COHERENT, Libra, 0.03 W, 80 fs, 2 kHz). The SHG signal was detected with a photomultiplier tube (Hamamatsu H7926). The sample pellet was cooled and heated at a rate of 3.5 K in a cryostat. The results are shown in **Figure S6**.

6 X-ray Absorption Near Edge Spectroscopy

X-ray Absorption Near Edge Spectroscopy **(**XANES) data were collected on beam line X-19A at Brookhaven NSLS. Mn and Fe XANES were recorded with a Si-111 double crystal monochromator in both transmission and fluorescence modes with simultaneous standards. The W XANES was collected in fluorescence mode in a He-atmosphere-chamber with standards run.

The main edge features at 3*d* transition metal K-edges are dominated by 1*s* to 4*p* transitions, riding on a step-feature continuum onset. Despite substantial variations/energy-splittings in the main edge features the chemical shift (to higher energy with increasing valence) of the K edge has been widely used to chronicle the evolution of the transition metal valence state in oxide-based materials.[1, 4, 14-18] In **Figure S7**a the Mn-K main edge for Mn_2FeWO_6 is compared to the spectra for the standards: $Mn^{2+}O$ (NaCl structure with edge sharing octahedra),[14] the perovskite based $LaMn^{3+}O_3$ and $CaMn^{4+}O_3$ (with corner sharing octahedra),[17] and $Mn^{2+}{}_2FeTaO_6$ (LN-type structure with face- edge- and corner-sharing of the octahedra).[4] The low chemical shift of the Mn_2FeWO_6 spectrum, and its close resemblance to that of the $Mn^{2+}{}_2FeTaO_6$ standard spectrum, confirms the formal Mn^{2+} valence in the former. **Figure S7**b shows the Mn-K pre-edges for the same series of compounds. The pre-edge features at the K-edges of 3*d* transition metal compounds are due to quadrupole allowed 1*s*/3*d* or dipole allowed 1*s*/3*d*-*p*-hybridized transitions. The structure and energy shift of the pre-edge features can offer a second method of identifying the transition metal valence. [2,26-31] In the pre-edge region a1, b1-b2, and c1-c2-c3 structures change and shift up in energy between the Mn^{2+}, Mn^{3+} and Mn^{4+} standards. The Mn-pre-edge of Mn_2FeWO_6 has a low chemical shift a1 feature, typical of the Mn^{2+} standards. This is again consistent with the nominal Mn^{2+} assignment in this compound. It is worth noting that there is a second feature (d in **Figure** S7b) that is characteristically split to higher energy in the pre-edge of this compound. This feature presumably involves *d*-states on a neighboring site since it lies closer

to the main edge onset, and would not involve an on-site core-hole Coulomb interaction energy.

In **Figure S7**c the Fe-K main edge for Mn_2FeWO_6 is compared to the spectra for the standards: $Fe^{2+}O$, $LiFe^{2+}PO_4$, $LaSrFe^{3+}TiO_6$, $LaSrFe^{3+}O_4$, $Zn_2Fe^{3+}TaO_6$ [1] and $SrFe^{\sim 4+}O_{3-\delta}$. The chemical shift of the Mn_2FeWO_6 spectrum clearly falls well below those of the Fe^{3+} standards. With the caveat that the Fe chemical shift is somewhat higher than the other Fe^{2+} standard spectra, a nominal Fe^{2+} valence in Mn_2FeWO_6 is consistent with the main-edge Fe XANES results. **Figure S7**d shows the Fe-K pre-edges for the same series of compounds and its background are similar to the Mn pre-edge discussion above. In the Fe-K pre-edge region bimodal a1-a2, b1-b2, and c1-c2 structures change and shift up in energy for the Fe^{2+}, Fe^{3+} and $Fe^{\sim 3+}$ standards, respectively. The Mn_2FeWO_6 pre-edge has a low chemical shift a1 feature typical of the Fe^{2+} standards (similar to the Mn-K case). This is again consistent with the nominal Fe^{2+} assignment in this compound. A second higher energy feature labeled "d" is again present in analogy to the Mn-K pre-edge results on this compound.

The intense peak features at the L_3-edges of 4*d*/5*d* transition metals (T) involve 2*p*-core to 4*d*/5*d* final-state transitions.[1, 4, 12, 15, 19-21] These features can provide a probe of the empty 4*d* state energy distribution, albeit modified by the transition matrix element, core–hole interaction and multiplet effects. In octahedral coordination the transition metal *d*-states are split into lower energy, t_{2g} (sextet) and a higher energy e_g (quartet) states. In low-*d*-occupancy transition metals (e.g. Ta - W - Re), the T L_3-edges display a robust two peak structure with the lower energy peak (A) involving transitions into empty t_{2g} states (see **Figure S7**e and **Figure S7**f inset); and the high-energy peak (B) involving excitations into empty e_g states. For *d*-hole counts greater than 4 the B-feature intensity reflects the empty e_g states and the intensity of the A-feature scales with the number of t_{2g}-holes.[2,25,27,28,32-34] Thus the A-feature intensity, relative to that of the B-feature, provides an indicator of the T 5*d* count/valence state. This effect is well illustrated in **Figure S7**e where a comparison of the T L_3-edges of ~ $5d^0$

and ~ $5d^1$ standards has been made. In the ~ $5d^0$ compounds (W^{6+} and Ta^{5+}), the peak intensity of the A-feature is more intense, and in the ~ $5d^1$ compound (Re^{6+}), it is less intense than the B-feature.[2,25,27,28,32-34] **Figure S7**f shows the W L_3-edges for Mn_2FeWO_6, the $Sr_2MnW^{6+}O_6$ (perovskite structure) standard, elemental W (for reference). In the expanded energy inset of **Figure S7**f the relative A-feature intensity for the Mn_2FeWO_6 spectrum indicates a nominal W^{6+} (~ d^0) configuration.[12] It is worth noting: that the A-B feature splitting is smaller in Mn_2FeWO_6 than in the perovskite standard; and that the overall chemical shift (reflected by the center of the A-B features) is somewhat smaller in Mn_2FeWO_6 possibly indicating some retention of *d*-charge. In the main portion of **Figure S7**f an expanded view of the x-ray absorption fine structure oscillations above the W-L_3 edge is shown. The C-feature indicated in the figure can be viewed as a continuum resonance caused by the O-ligand-shell or equivalently as the first extended x-ray absorption fine structure oscillation (enhanced by multiple scattering effects).[19-20] In either case the energy of the C-feature, relative to the edge, has been shown to reflect the average radius of the O-ligand-shell. In **Figure S7**f the C-feature of Mn_2FeWO_6 can be seen to be shifted to lower energy relative to that of the Sr_2MnWO_6 indicating a W-O bond length expansion. This expansion could also indicate some retention of *d*-charge at the W-site.

7. Magnetic Properties

Magnetization measurements were carried out with a commercial Quantum Design superconducting quantum interference device (SQUID, up to 7 T) magnetometer and a physical property measurement system (PPMS, up to 14 T). The magnetic susceptibility was measured in zero field cooled (ZFC) and field cooled (FC) conditions under 0.01-14 T magnetic field, at temperatures ranging from T = 5 to 400 K. Isothermal magnetization curves were obtained at T = 5-400 K under an applied magnetic field that varied from -14 to 14 T.

The dielectric properties were measured with a NovoControl-Alpha frequency response analyzer.

Figure S8a shows selected linear $M(T)$ curves. The derivative dM/dT are shown in the inset. The H = 1 T curve manifests a clear peak-type antiferromagnetic transition anomaly. In the H = 1 T dM/dT curve, one notes a broad negative peak percussive to the transition indicating the onset of antiferromagnetic (AFM) correlations above the ordering temperature. In the H = 7 T, $M(T)$ curve a FC/ZFT disparities at temperatures up to almost 30 K indicate the presence of antiferromagnetic domains. The H = 7, 10, and 14 T dM/dT curves also show broad negative peaks suggestive of AFM correlations in the 75 K energy range (A4 in figure), which is close to the low-field antiferromagnetic ordering temperature. This suggests antiferromagnetic correlations in the paramagnetic (PM) region at these higher fields.

8. Dielectric and Polarization Measurements

The ferroelectric P-E loops were recorded with a modified Sawyer-Tower circuit employing a Keithley 6517 electrometer. The samples were sandwiched between Ag paste deposited electrodes, in parallel plate geometry for the above measurements. Mn_2FeWO_6 exhibits poor dielectric characteristic with large and frequency-dependent relative permittivity and loss (**Figure S11**a). At higher temperature, the conductivity is dominated by two steps that are caused by contact effects and are not intrinsic. The conductivity is reduced at lower temperatures, where ε' at the different frequencies merge to ~ 20 (inset of **Figure S11**a, top figure). There is no sharp, divergence-like anomaly in ε' as expected for ferroelectric (FE) transitions in the range up to 300 K. Further experiments to measure the polarization directly with dielectric pulse (known as PUND,[22] **Figure S11**b) and P(E) (**Figure S11**c) measurements[23] show only conductivity at and above 70 K, which is reduced with temperature. No switchable polarization was observed down to 5 K. Thus, ferroelectricity is not demonstrated by these measurements as the structural polarity is not switchable by

external fields. Further measurements need to be conducted on mono-domain samples, such as thin film or single crystal, since it is well known that switchable signals could be cancelled between the pinned domain walls in compact polycrystalline specimen.[24-25]

9. First-Principles Calculations

The first-principles spin-polarized calculations for Mn_2FeWO_6 were performed in the context of density-functional theory (DFT) with the Vienna *Ab-initio* Simulation Package (VASP)[26] using the generalized-gradient approximation parameterized by the Perdew-Burke-Ernzerhof (PBE) functional.[27] The wave functions were expanded in a plane-wave basis with a cutoff energy of 520 eV for the projector-augmented-wave (PAW) valence electrons.[28] For the localized *d* orbitals of Mn and Fe atoms, a Hubbard *U* of 4.2 eV[2,3] was applied with the Dudarev DFT+U approach.[29] A 4 × 4 × 4 Monkhorst-Pack *k*-point mesh was generated to sample the Brillouin zone.[30] The spontaneous polarization was calculated with the Berry-phase formalism.[31]

Supplementary Figures

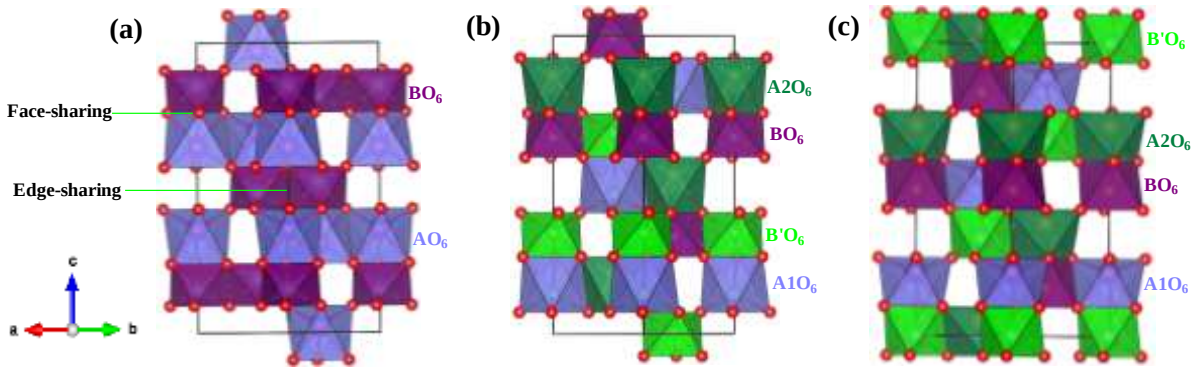

Supplementary Figure S1. Comparison of the crystal structures of the $A_2BB'O_6$-type corundum family with space group *R*-3 or *R*3, which consist of face-sharing AO_6/BO_6 octahedral dimer pairs along the *c*-axis and edge-sharing octahedral pairs in the *ab*-plane. (a) The ilmenite (IL) structure with disordered arrangment of the B- and B'-site cations and alternating edge-sharing $BO_6/B'O_6$ and AO_6 octahedral layers in the ab-plane. (b) The ordered ilmenite (OIL) structure with layers of edge-sharing $A1O_6/A2O_6$ octahedra alternating with edge-sharing $BO_6/B'O_6$ layers. (c) The Ni_3TeO_6 (NTO) structure with ordered B- and B'-site cations and alternating edge-sharing $A1O_6/BO_6$ and $A2O_6/B'O_6$ octahedral dimers in the ab-plane.

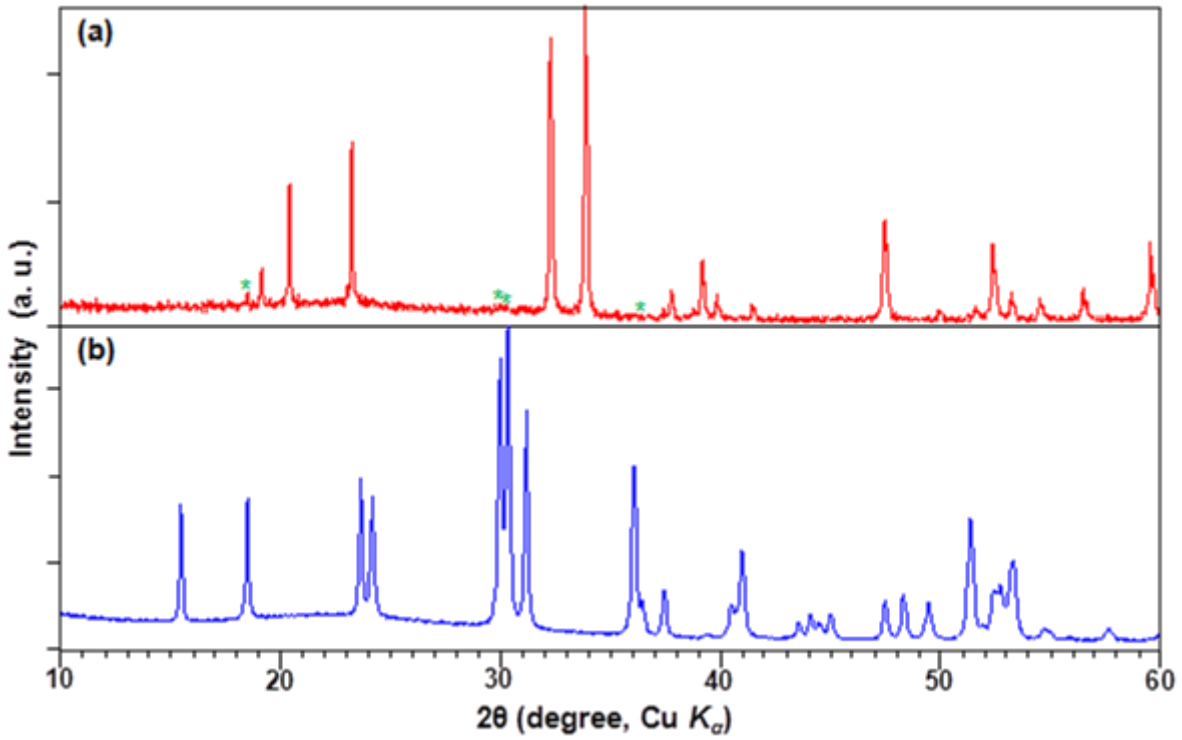

Supplementary Figure S2. Lab PXD patterns of the (a) as-made Mn_2FeWO_6 and (b) $(Mn_{0.8}Fe_{0.2})WO_4$ wolframite phase prepared at the same condition. Asterisks (*) in (a) indicate peaks of the very small wolframite impurity in the as-made material. The $(Mn_{0.8}Fe_{0.2})WO_4$ wolframite phase (*P*2/*c*, a ~ 4.81 Å, b ~ 5.75 Å, c ~ 4.99 Å, β = 90.89º) was prepared to evaluate its contribution to the physical properties of the as-made materials.

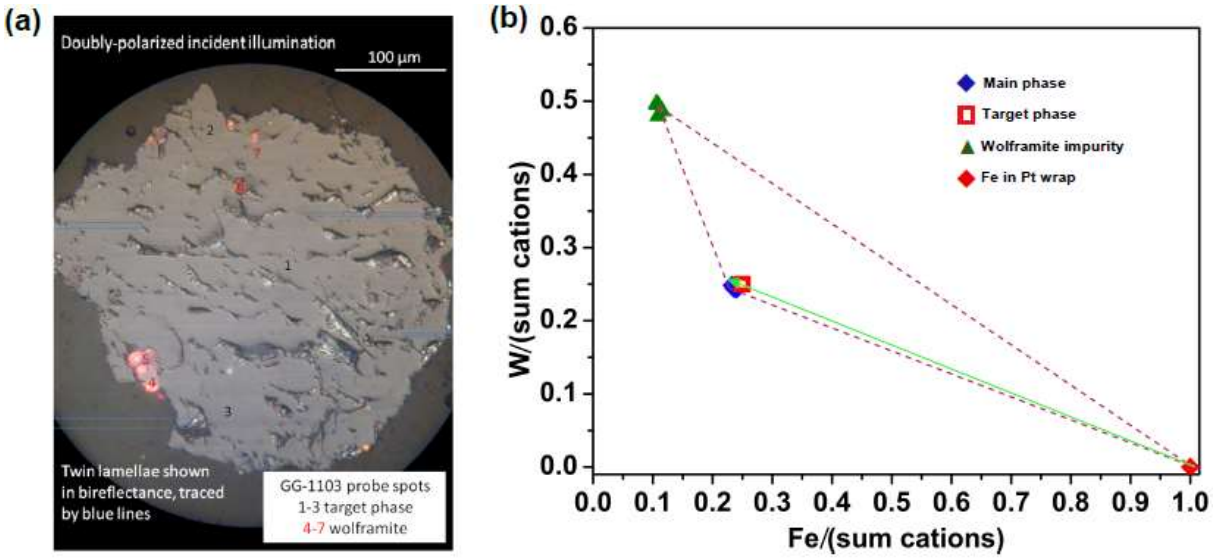

Supplementary Figure S3. Optical and microprobe analysis. (a) Doubly-polarized incident illumination image on Mn_2FeWO_6 target composition clearly shows a large twinned single crystal of the target phase with small impurity phases of hübnerite-rich wolframite composition $(Mn,Fe)WO_4$ that can display prominent red-orange internal reflections. Twin lamellae of the target phase are shown in bi-reflectance traced by blue lines. The black (1-3) and red (4-7) numbers correspond to the microprobe analysis spots on target and impurity phases, respectively given in **Table S1**. GG-1103 is the high pressure run sequence number. (b) Comparison of the observed Fe and W content in the main and impurity phases, showing that the main phase is close to the target Mn_2FeWO_6. Trace Fe was detected in the Pt-wrap. Green arrow shows that mass balance between the target composition and the Fe-deficient wolframite + target phase assemblage can be closed by Fe-depletion to the Pt wrap. The proportions of impurity wolframite and target phase observed are in good agreement with the mass balance. The distribution of wolframite near the edges of the specimen is consistent with the Fe-loss to the exterior Pt wrapping.

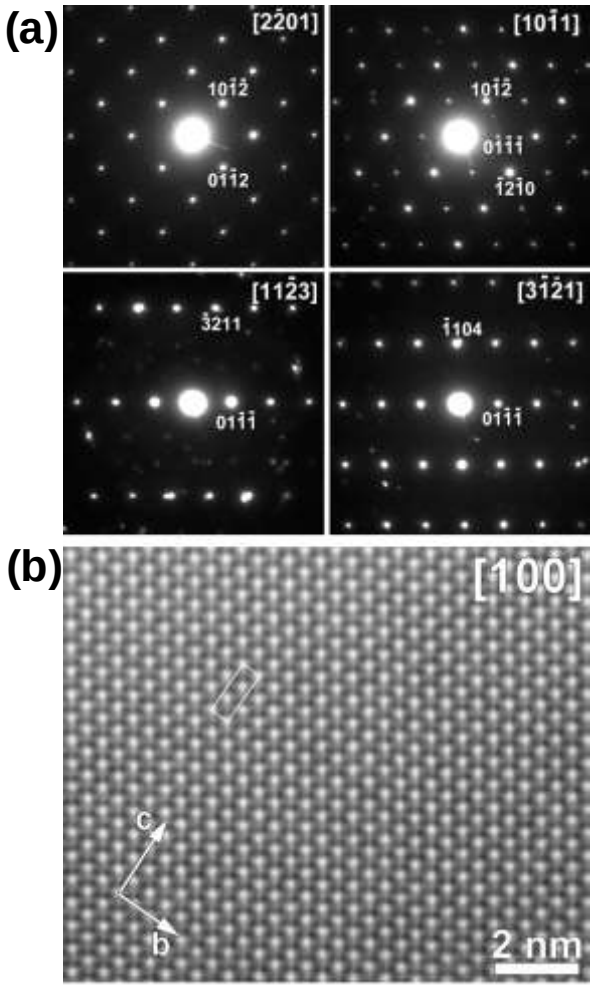

Supplementary Figure S4. Electron diffraction image of Mn_2FeWO_6. (a) Representative selected area electron diffraction tilt patterns of Mn_2FeWO_6, around the reciprocal directions $[10\bar{1}\bar{2}]$ and $[01\bar{1}\bar{1}]$, showing a match with the cell parameters from PXD results (b) HAADF-STEM image of Mn_2FeWO_6 projected along [100]. the white rectangle shows the close up area in **Figure 1**b.

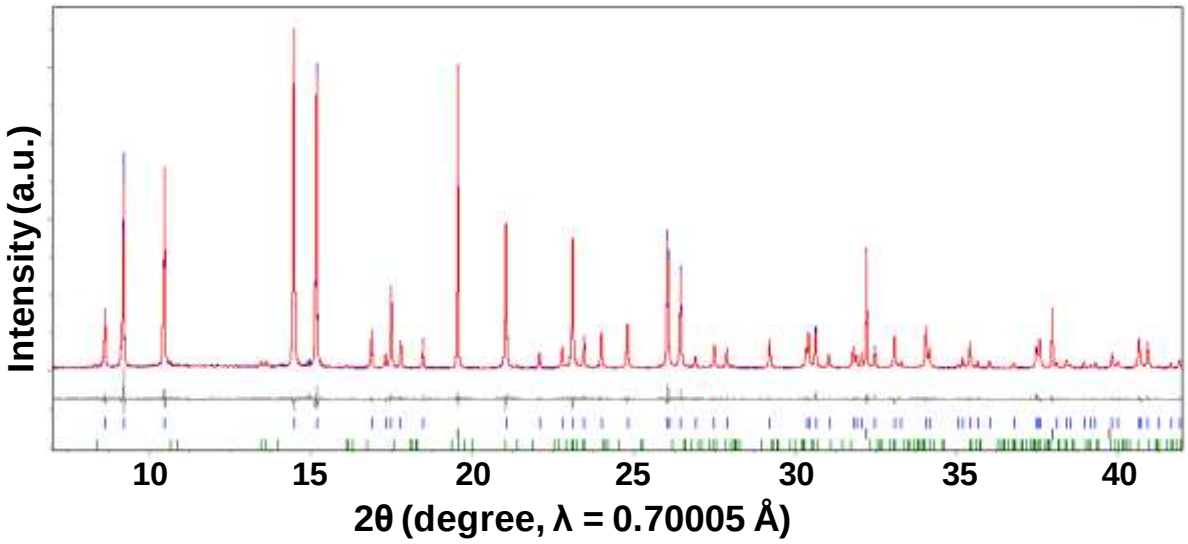

Supplementary Figure S5. Experimental, calculated, and difference of the SPXD patterns of Mn_2FeWO_6 at RT, corresponding to the refinements in NTO-type structure. The vertical bars (|) show the peak index of Mn_2FeWO_6, diamond (internal standard), and the wolframite impurity, respectively, from top to bottom.

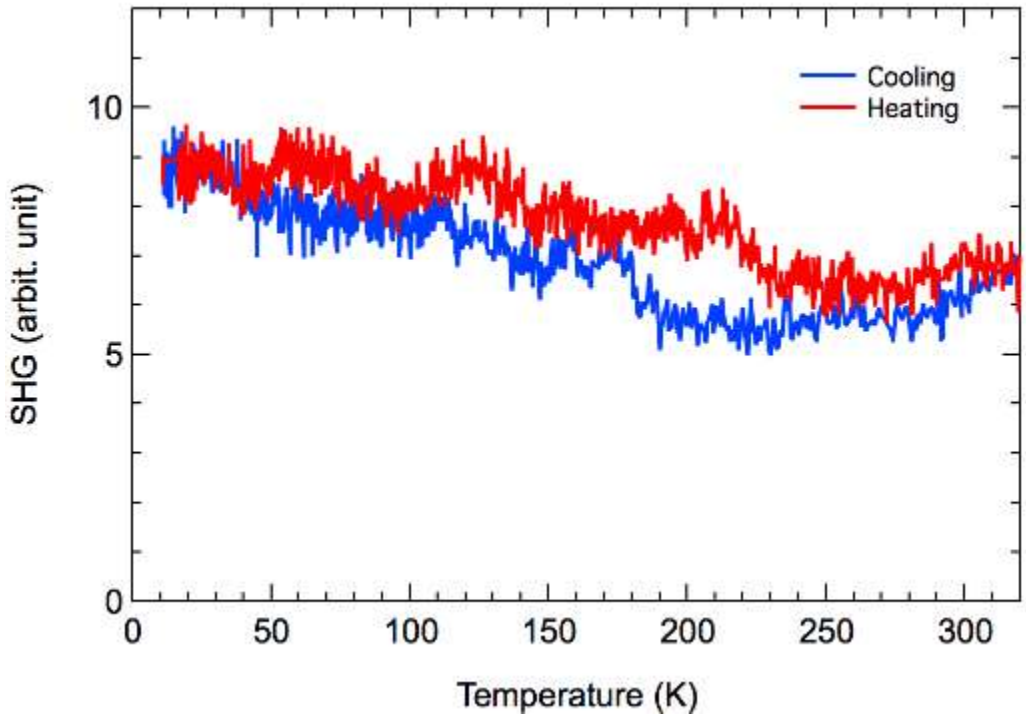

Supplementary Figure S6. Temperature dependence of optical SHG was measured for a Mn_2FeWO_6 pellet between 10 and 300 K. The measurements were performed in normal incidence reflection geometry using an 800 nm fundamental input generated by a Ti:sapphire laser (COHERENT, Libra, 0.03 W, 80 fs, 2 kHz). The SHG signal was detected with a photomultiplier tube (Hamamatsu H7926). The sample was cooled and heated at a rate of 3.5 ^{o}C/min in a cryostat. Finite SHG signals were observed in the whole measurement temperature range, indicating noncentrosymmetry of the present material. The SHG intensity gradually increases as temperature is decreased, and indicates a possible anomaly ~ 200-250 K.

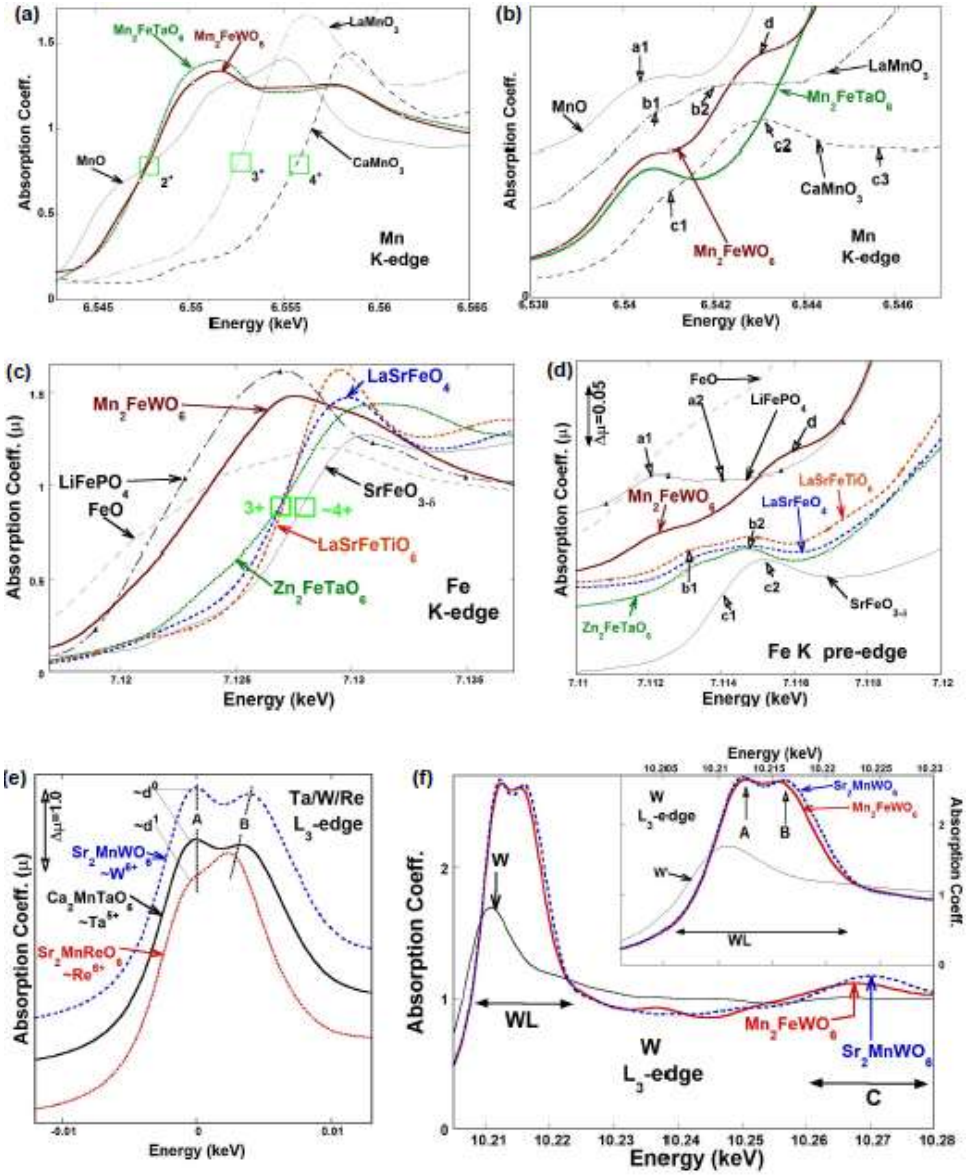

Supplementary Figure S7. XANES spectroscopy of Mn_2FeWO_6. (a) The Mn-K edge and (b) pre edge spectra for the Mn_2FeWO_6 compound, and a series of octahedral O-coordinated standard Mn compounds with varying formal valences: $Mn^{2+}O$, $Mn^{2+}{}_2FeTO_6$, $LaMn^{3+}O_3$, and $CaMn^{4+}O_3$**;** (**c**) The Fe-K edge and (d) pre edge spectra for the Mn_2FeWO_6 compound, and a series of octahedral O-coordinated standard Fe compounds with varying formal valences: $Fe^{2+}O$, $LiFe^{2+}PO_4$, $LaSrFe^{3+}TiO_6$, $LaSrFe^{3+}O_4$, $Zn_2Fe^{3+}TaO_6$ and $SrFe^{\sim 4+}O_{3-\delta}$; (e) The A-B features for $5d^0$, W^{6+}/Ta^{5+} compounds and a $5d^1$, Re^{6+} compound; (f) The W L_3-edges for Mn_2FeWO_6, and the $Sr_2MnW^{6+}O_6$ standard on an energy scale showing the continuum resonance C-features. Inset: an expanded view of the A-B "white line" (WL) features.

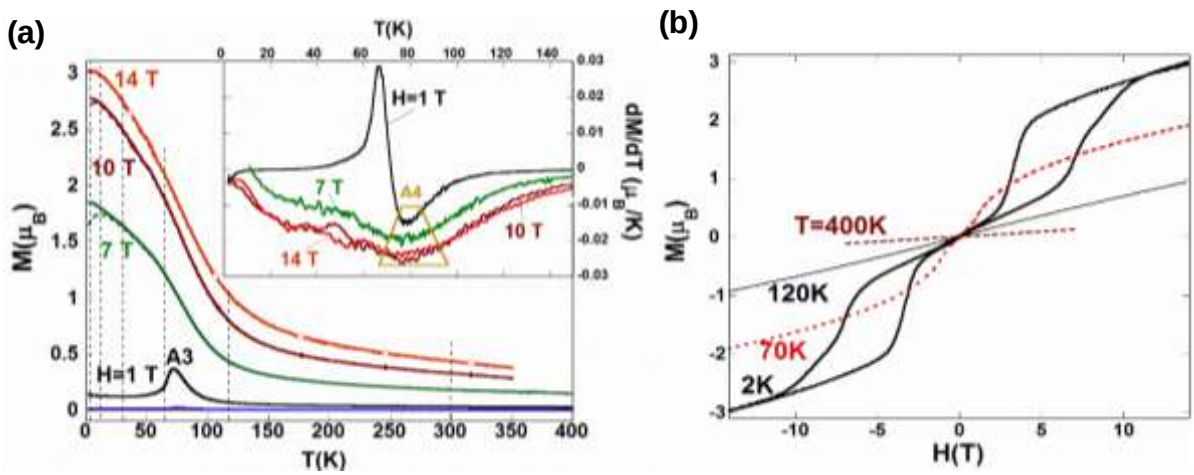

Supplementary Figure S8. Magnetism of Mn_2FeWO_6. (a) Magnetization (*M*) *vs.* temperature (*T*) curves at a series of fields between 1 and 14 T. The ZFC and FC curves, respectively are dashed and solid lines at each field. Inset shows the derivative of the *M*(*T*) curves, d*M*/d*T*, for *H* = 1, 7, 10 and 14 T. Note the negative inflection peak identified by the A4 in the derivative plots. (b) Selected full magnetization *M*(*H*) loops, *M vs.H* (between -14 and 14 T) at 2, 70, 120, and 400 K illustrating the various behaviors.

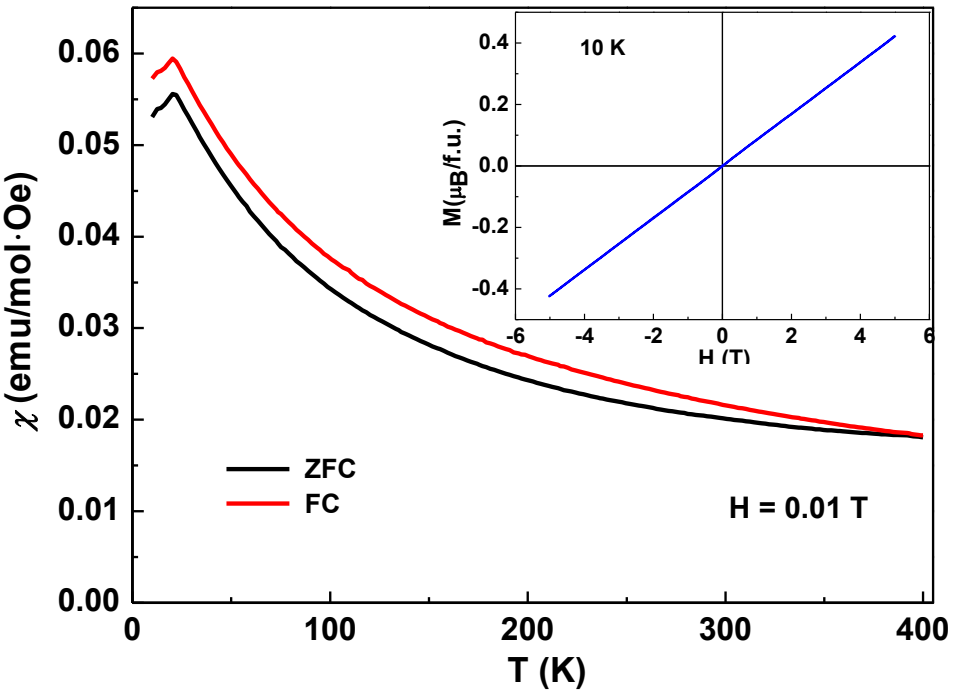

Supplementary Figure S9. Susceptibility (χ) *vs.* temperature (*T*) plots of $(Mn_{0.8}Fe_{0.2})WO_4$ in the ZFC as well as FC modes from 5 to 400 K with H = 0.01 T. Inset shows the magnetization (*M*) *vs.* field (*H*) curves between -5 and 5 T at 10 K.

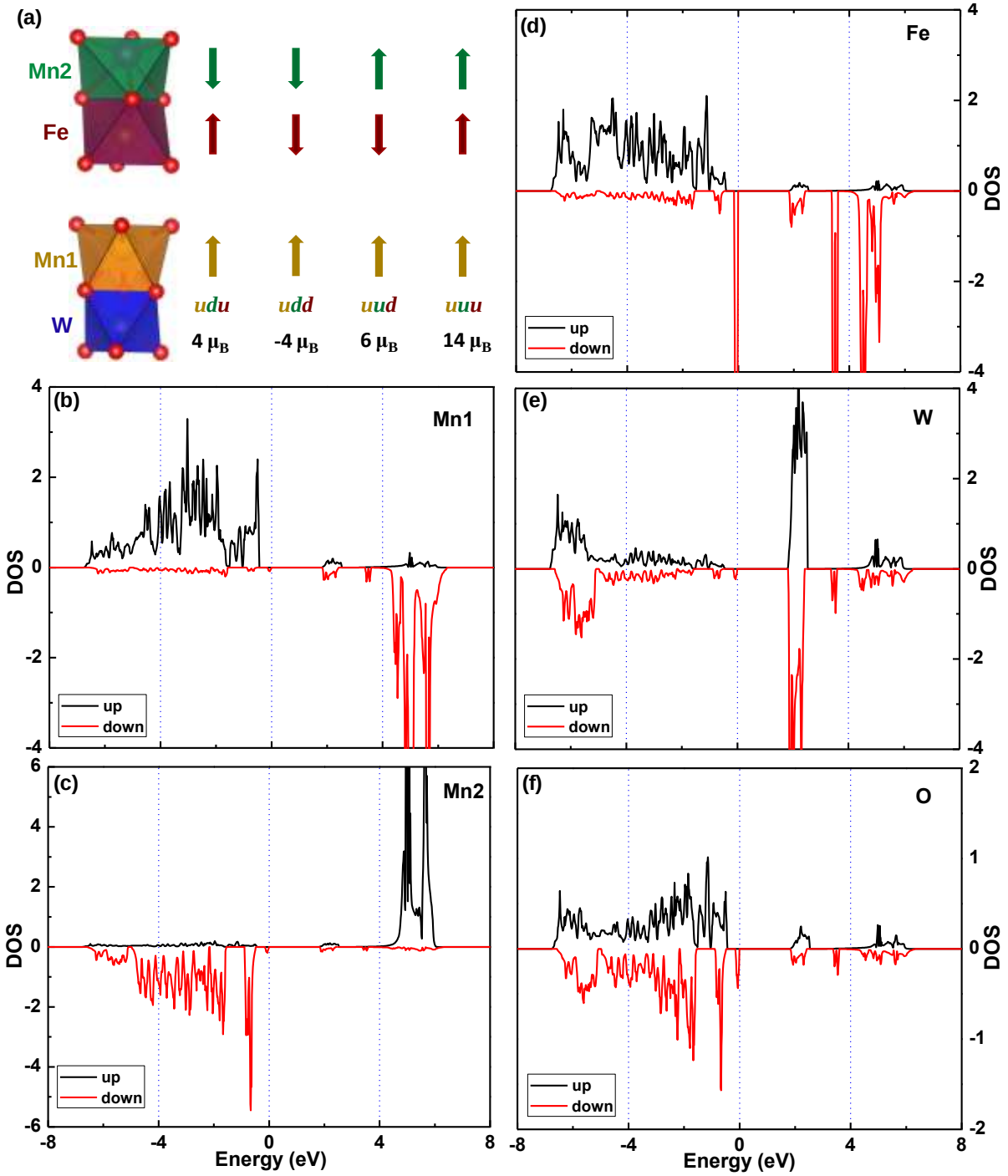

Supplementary Figure S10. DFT calculations results. (a) Possible magnetic structures and DFT calculations of DOS in the ground state (up-down-up, *udu* in (a)) magnetic configuration projected to (b) Mn1, (c) Mn2, (d) Fe, (e) W, and (f) O sites. This *udu* magnetic configuration is found to be energetically favorable over the ferrimagnetic (*udd* and *uud*) and ferromagnetic (*uuu*) configurations.

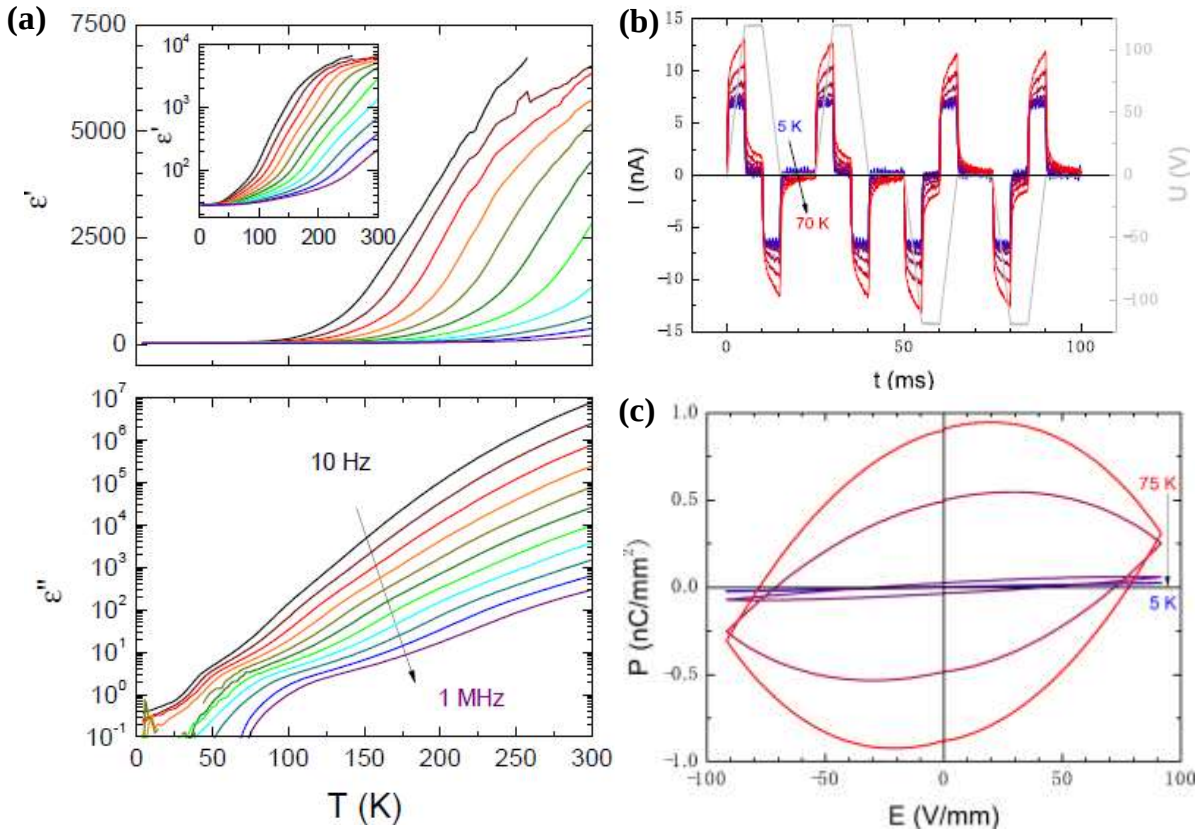

Supplementary Figure S11. Dielectric and polarization measurements. (a) Temperature dependence of the dielectric permittivity ε' (top) and loss ε" (bottom) as measured for frequency between 10 and 10^6 Hz; (b) long time pulse dielectric measurements on up to 70 K; (c) P(E) loop measured between 5 and 75 K as measured with triangular field ramping. The parabolic shape of the curves at higher temperatures can be understood due to ohmic conductivity and is not connected to polarization switching.

Supplementary Tables

Table S1 Microprobe analysis atomic % on different spots in **Figure S 3**a

Spot	Mn	Fe	W	O	Total
#1	23.1	10.5	10.8	55.6	100.0
#2	23.2	10.8	10.9	55.1	100.0
#3	23.1	10.4	11.1	55.5	100.0
#4	15.0	4.0	18.7	62.4	100.0
#5	15.1	4.1	18.9	61.8	100.0
#6	14.1	3.7	16.4	65.7	100.0
#7	15.1	4.4	18.4	62.1	100.0

Table S2. Comparison of the structure parameters of Mn_2FeWO_6 from SPXD data refinements (first line) and DFT calculations based on udu ordering ground state (second line), respectively.

Atom	Site	*x*	*y*	*z*	B (Å^2)
Mn1	3*a*	0	0	0.2146(2)	0.48(4)
				0.2163	
Mn2	3*a*	0	0	0.7216(2)	0.53(4)
				0.7181	
Fe	3*a*	0	0	0.5066(5)	0.53(4)
				0.4950	
W	3*a*	0	0	0	0.26(1)
				0.0043	
O1	9*b*	0.2735(15)	-0.0194(18)	0.0958(7)	0.15(17)
		0.275371	-0.020974	0.0972	
O2	9*b*	0.6532(15)	-0.0510(15)	0.6020(7)	0.26(16)
		0.655282	-0.048350	0.6034	

Space group *R3* (146), $Z = 3$. SPXD: $a = 5.29657(1)$ Å, $c = 13.93915(6)$ Å, $V = 338.65(1)$ Å^3, $R_p/R_{wp} = 5.05/6.39\%$, Gof = 1.68. DFT calculations: $a = 5.3739$ Å, $c = 14.0653$ Å, $V = 351.78$ Å^3. B is the isotropic atomic displacement parameter.

Table S3 Selected interatomic distances (Å), bond valence sums (BVS), octahedral distortion parameters (Δ), and bond angles (º) in NTO-type Mn_2FeWO_6 at room temperature

$Mn1O_6$		**FeO_6**	
Mn1-O1 × 3	2.236(8)	Fe-O1 × 3	2.135(11)
-O2 × 3	2.138(9)	-O2 × 3	2.172(10)
<Mn1-O>	2.187(9)	<Fe-O>	2.154(10)
BVS	2.07	BVS	1.93
ΔMn1 ($\times 10^{-4}$)	5.02	ΔFe ($\times 10^{-4}$)	0.74
$Mn2O_6$		**WO_6**	
Mn2-O1 × 3	2.064(6)	W-O1 × 3	2.01(1)
-O2 × 3	2.393(9)	-O2 × 3	1.840(8)
<Mn2-O>	2.228(6)	<W-O>	1.925(9)
BVS	2.02	BVS	6.03
ΔMn2 ($\times 10^{-4}$)	54.5	ΔW ($\times 10^{-4}$)	19.5
Mn1-W	2.991(4)	Mn2-Fe	2.996(7)
Mn1-Fe	3.112(2)	Mn2-W	3.152(1)
O1-Mn1-O1	71.2(3)	O1-Fe-O1	96.7(4)
O2-Mn1-O2	108.3(3)	O2- Fe-O2	86.4(3)
O1-Mn1-O2	86.1(3)	O1- Fe-O2	87.8(3)
	87.8(3)		88.6(3)
	152.8(3)		172.6(4)
O1-Mn2-O1	112.7(3)	O1-W-O1	80.7(3)

O2-Mn2-O2	76.9(3)	O2-W-O2	98.0(3)
O1-Mn2-O2	73.8(3)	O1-W-O2	88.4(4)
	89.6(3)		91.6(3)
	149.8(3)		167.5(3)

Table S4 Comparison of the crystallographic data of Mn_2FeWO_6 and related Mn_2FeMO_6 (M = Sb^{5+}, Nb^{5+}, Ta^{5+}, Mo^{5+}) analogs at room temperature.

Compounds	**Mn_2FeSbO_6**	**Mn_2FeNbO_6**	**Mn_2FeTaO_6**	**Mn_2FeMoO_6**	**Mn_2FeWO_6**
Space Group	*R-3*	*R3c*	*R3c*	*R3*	*R3*
a/Å	5.226	5.2740	5.2721	5.2505	5.2966
c/Å	14.325	13.9338	13.8892	13.8355	13.9392
V/Å3	338.82	335.65	334.33	330.3	338.65
<Mn1-O>/Å	2.212	2.155	2.215	2.195	2.187
<Mn2-O>/Å[a]	-	-	-	2.195	2.228
<Fe-O>/Å[b]	2.006	2.035	2.01	2.033	2.154
<M-O>/Å*b*	2.006	2.035	2.01	2.008	1.925
r(M)/Å[c,[32]]	0.60	0.64	0.64	0.61	0.60
BVS (Mn1)[d]	2.01/2	2.08/2	1.94/2	2.08/2	2.07/2
BVS (Mn2)[d]	-	-	-	2.08/2	2.02/2
BVS (Fe)[d]	3.10/3	2.89/3	3.05/3	3.10/3	1.93/2

BVS (M)[d]	5.08/5	4.35/5	4.71/5	4.56/5	6.03/6
Ref.	[8]	[4]	[4]	[3]	This work

[a] only one Mn position in *R-3* and *R3c* symmetries; [b] Fe and M are disordered in *R-3* and *R3c* symmetries, thus have the same <Fe-O> and <M-O> for each compound; [c] Ionic radii of Sb^{5+}, Nb^{5+}, Ta^{5+}, Mo^{5+}, and W^{6+} in octahedral coordination; [d] Both the calculated/observed BVS are listed for comparison.

Table S5 Magnetic energies (relative to unrelaxed *udu*) and nominal total magnetic moments per formula unit for FiM orderings having the periodicity of the primitive structural unit cell. ΔE_1 is for energies evaluated at the unrelaxed experimental coordinates, while ΔE_2 applies to energies calculated after relaxation of the internal coordinates.

Magnetic ordering	***uuu***	***uud***	***udu***	***udd***
Edge sharing Mn_1-Fe coupling	FM	AFM	FM	AFM
Face sharing Mn_2-Fe coupling	FM	AFM	AFM	FM
ΔE_1 (meV/ f.u.)	83	27	0	26
ΔE_2 (meV/ f.u.)	-95	-190	-220	-181

Table S6 Magnetic energies (relative to unrelaxed *udu*) for AFM orderings in doubled unit cells. ΔE_1 is for energies evaluated at the unrelaxed experimental coordinates, while ΔE_2 applies to energies calculated after relaxation of the internal coordinates.

Magnetic ordering	***udd-duu***	***udu-dud***	***udu-udd***	***uud-ddu***	***uuu-ddd***
ΔE_1 (meV/ f.u.)	40	12	11	-3	48
ΔE_2 (meV/ f.u.)	-208	-225	-233	-229	-214

References

[1] M.-R. Li, P. W. Stephens, M. Retuerto, T. Sarkar, C. P. Grams, J. Hemberger, M. C. Croft, D. Walker, M. Greenblatt, *J. Am. Chem. Soc.* **2014**, *136*, 8508-8511.

[2] D. Walker, M. A. Carpenter, C. M. Hitch, *Am. Mineral.* **1990**, *75*, 1020-1028.

[3] M.-R. Li, M. Retuerto, D. Walker, T. Sarkar, P. W. Stephens, S. Mukherjee, T. S. Dasgupta, J. P. Hodges, M. Croft, C. P. Grams, J. Hemberger, J. Sánchez-Benítez, A. Huq, F. O. Saouma, J. I. Jang, M. Greenblatt, *Angew. Chem. Int. Ed.* **2014**, *53*, 10774-10778.

[4] M.-R. Li, D. Walker, M. Retuerto, T. Sarkar, J. Hadermann, P. W. Stephens, M. Croft, A. Ignatov, C. P. Grams, J. Hemberger, I. Nowik, P. S. Halasyamani, T. T. Tran, S. Mukherjee, T. S. Dasgupta, M. Greenblatt, *Angew. Chem. Int. Ed.* **2013**, *52*, 8406-8410.

[5] A. P. Young, C. M. Schwartz, *Science* **1963**, *141*, 348-349.

[6] N. L. Bowen, J. F. Schairer, *Am. J. Sci.* **1932**, *Series 5 Vol. 24*, 177-213.

[7] A. Coelho, *J. Appl. Crystallogr.* **2000**, *33*, 899-908.

[8] P. B. Moore, *Am. Mineral.* **1968**, *53*, 6.

[9] G. King, S. Thimmaiah, A. Dwivedi, P. M. Woodward, *Chem. Mater.* **2007**, *19*, 6451-6458.

[10] G. King, L. M. Wayman, P. M. Woodward, *J. Solid State Chem.* **2009**, *182*, 1319-1325.

[11] C. De, T. H. Kim, K. H. Kim, A. Sundaresan, *PCCP* **2014**, *16*, 5407-5411.

[12] M. Retuerto, M. R. Li, A. Ignatov, M. Croft, K. V. Ramanujachary, S. Chi, J. P. Hodges, W. Dachraoui, J. Hadermann, T. T. Tran, P. S. Halasyamani, C. P. Grams, J. Hemberger, M. Greenblatt, *Inorg. Chem.* **2013**, *52*, 12482-12491.

[13] R. Mathieu, S. A. Ivanov, G. V. Bazuev, M. Hudl, P. Lazor, I. V. Solovyev, P. Nordblad, *Appl. Phys. Lett.* **2011**, *98*, 202505.

[14] M.-R. Li, M. Retuerto, Y. Bok Go, T. J. Emge, M. Croft, A. Ignatov, K. V. Ramanujachary, W. Dachraoui, J. Hadermann, M.-B. Tang, J.-T. Zhao, M. Greenblatt, *J. Solid State Chem.* **2013**, *197*, 543-549.

[15] M. Retuerto, M. R. Li, Y. B. Go, A. Ignatov, M. Croft, K. V. Ramanujachary, R. H. Herber, I. Nowik, J. P. Hodges, W. Dachraoui, J. Hadermann, M. Greenblatt, *J. Solid State Chem.* **2012**, *194*, 48-58.

[16] A. Sahiner, M. Croft, S. Guha, I. Perez, Z. Zhang, M. Greenblatt, P. A. Metcalf, H. Jahns, G. Liang, *Phys. Rev. B* **1995**, *51*, 5879-5886.

[17] M. Croft, D. Sills, M. Greenblatt, C. Lee, S. W. Cheong, K. V. Ramanujachary, D. Tran, *Phys. Rev. B* **1997**, *55*, 8726-8732.

[18] T. K. Mandal, A. M. Abakumov, J. Hadermann, G. Van Tendeloo, M. Croft, M. Greenblatt, *Chem. Mater.* **2007**, *19*, 6158-6167.

[19] G. Popov, M. Greenblatt, M. Croft, *Phys. Rev. B* **2003**, *67*, 024406.

[20] Q. Lin, M. Greenblatt, M. Croft, *J. Solid State Chem.* **2005**, *178*, 1356-1366.

[21] T. K. Mandal, V. V. Poltavets, M. Croft, M. Greenblatt, *J. Solid State Chem.* **2008**, *181*, 2325-2331.

[22] J. F. Scott, *Ferroelectric Memories, Springer, Berlin* **2000**, Ch. 6.

[23] M. Fukunaga, Y. Noda, *J. Phys. Soc. Jpn.* **2008**, *77*, 064706.

[24] D. Lebeugle, D. Colson, A. Forget, M. Viret, *Appl. Phys. Lett.* **2007**, *91*, -.

[25] J. F. Scott, *J. Phys.: Condens. Matter* **2008**, *20*, 021001.

[26] G. Kresse, J. Furthmüller, *Phys. Rev. B* **1996**, *54*, 11169-11186.

[27] J. P. Perdew, K. Burke, M. Ernzerhof, *Phys. Rev. Lett.* **1996**, *77*, 3865-3868.

[28] G. Kresse, D. Joubert, *Phys. Rev. B* **1999**, *59*, 1758-1775.

[29] S. L. Dudarev, G. A. Botton, S. Y. Savrasov, C. J. Humphreys, A. P. Sutton, *Phys. Rev. B* **1998**, *57*, 1505-1509.
[30] H. J. Monkhorst, J. D. Pack, *Phys. Rev. B* **1976**, *13*, 5188-5192.
[31] R. D. King-Smith, D. Vanderbilt, *Phys. Rev. B* **1993**, *47*, 1651-1654.
[32] R. Shannon, *Acta Crystallogr. Sect. A* **1976**, *32*, 751-767.